Chinese Chemical Letters 36 (2025) 110099

Contents lists available at ScienceDirect

Chinese Chemical Letters

journal homepage: www.elsevier.com/locate/cclet

A mitochondria targeting Ir(III) complex triggers ferroptosis and autophagy for cancer therapy: A case of aggregation enhanced PDT strategy for metal complexes

Panpan Wang, Hongbao Fang*, Mengmeng Wang, Guandong Zhang, Na Xu, Yan Su*, Hongke Liu, Zhi Su*

Jiangsu Collaborative Innovation Center of Biomedical Functional Materials, College of Chemistry and Materials Science, Nanjing Normal University, Nanjing 210023, China

ARTICLE INFO

Article history:
Received 29 March 2024
Revised 4 June 2024
Accepted 6 June 2024
Available online 6 June 2024

Keywords:
Metal complex
AIEgens
Mitochondria targeting
Enhanced photodynamic therapy
Anticancer agent

ABSTRACT

Metal complexes hold significant promise in tumor diagnosis and treatment. However, their potential applications in photodynamic therapy (PDT) are hindered by issues such as poor photostability, low yield of reactive oxygen species (ROS), and aggregation-induced ROS quenching. To address these challenges, we present a molecular self-assembly strategy utilizing aggregation-induced emission (AIE) conjugates for metal complexes. As a proof of concept, we synthesized a mitochondrial-targeting cyclometalated Ir(III) photosensitizer Ir-TPE. This approach significantly enhances the photodynamic effect while mitigating the dark toxicity associated with AIE groups. Ir-TPE readily self-assembles into nanoaggregates in aqueous solution, leading to a significant production of ROS upon light irradiation. Photoirradiated Ir-TPE triggers multiple modes of death by excessively accumulating ROS in the mitochondria, resulting in mitochondrial DNA damage. This damage can lead to ferroptosis and autophagy, two forms of cell death that are highly cytotoxic to cancer cells. The aggregation-enhanced photodynamic effect of Ir-TPE significantly enhances the production of ROS, leading to a more pronounced cytotoxic effect. *In vitro* and *in vivo* experiments demonstrate this aggregation-enhanced PDT approach achieves effective *in situ* tumor eradication. This study not only addresses the limitations of metal complexes in terms of low ROS production due to aggregation but also highlights the potential of this strategy for enhancing ROS production in PDT.

Compared with other therapeutic methods, photodynamic therapy (PDT) is an important therapeutic method with minimal invasiveness, high spatiotemporal selectivity, and low toxicity to biological systems, which has shown great potential in clinical cancer treatment [1,2]. The efficiency of PDT depends on the high singlet oxygen ($^1O_2$) quantum yield of the photosensitizer (PS) to produce cytotoxic $^1O_2$ [3,4]. Under light irradiation, the used PSs can be activated to produce high reactive oxygen species (ROS), leading to apoptosis/necrosis or immune response [5,6]. Traditional PSs such as methylene blue, Rose Bengal, and porphyrin derivatives have been widely used in PDT [7]. Unfortunately, existing PSs usually suffer from poor photostability, low $^1O_2$ generation capacity, and $^1O_2$ quenching caused by aggregation, which limits their clinical application [8,9]. Despite significant endeavors to enhance the photophysical and photochemical characteristics of traditional PSs, no single photosensitizer capable of addressing all these issues has been identified to date. Hence, there is a pressing requirement to develop innovative photosensitizers with improved photodynamic attributes to elevate the efficacy of PDT.

Organometallic complexes, such as iridium (Ir), ruthenium (Ru), platinum (Pt), and gold (Au) complexes, show excellent $^1O_2$ generation capacity due to their long lifetime of triplet metal-ligand charge transition (^{3}MLCT) excited states [10-12]. However, ligands in Pt(II) and Au(III) complexes are unstable and may cause side effects at unexpected sites, whereas Ru(II) complexes have poor cell membrane penetration, resulting in long cellular uptake time and relatively high concentration requirements [13,14]. In contrast, Ir(III) complexes have attracted much attention as PSs due to their long triplet excited state lifetime, high $^1O_2$ quantum yield, tunable phosphorescence, and excellent cell permeability [15-17]. These features confer their potential for bioimaging and PDT applications. However, most Ir(III) complexes are hydrophobic, leading to a significant decrease in their photodynamic therapy efficacy in the hydrophilic environment of cellular systems [18-20]. Yang and his

* Corresponding authors.
E-mail addresses: fanghb@njnu.edu.cn (H. Fang), suyanahnu@163.com (Y. Su), zhisu@njnu.edu.cn (Z. Su).

https://doi.org/10.1016/j.cclet.2024.110099
1001-8417/

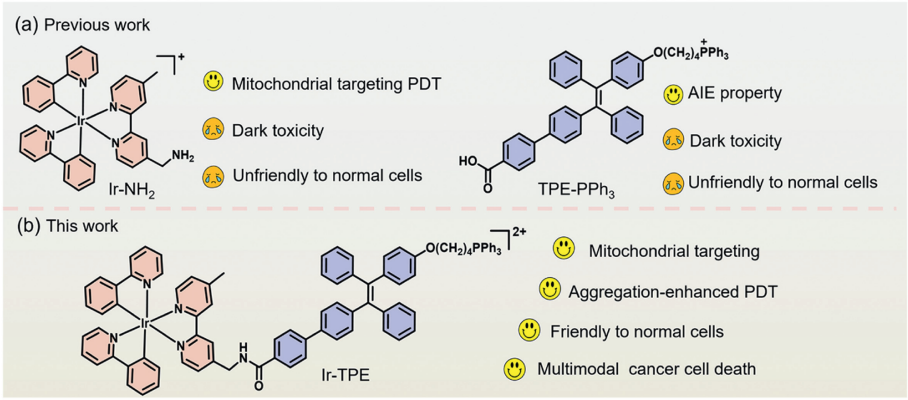

Scheme 1. The design of the mitochondria targeting aggregation-enhanced photosensitizer.

colleagues reported that Ir(III)-cyanine complex nanoparticles exhibited excellent photoacoustic imaging-guided PDT performance based on their hydrophobicity, but their efficiency in generating reactive oxygen species under aggregation was limited [21]. It is still desirable to develop a novel strategy to elevate the PDT efficacy of Ir(III)-based PS in aqueous solution.

It is well established in the literature that the enhanced intersystem crossing (ISC) efficiency of PSs is beneficial to improve $^1O_2$ production [22,23]. An effective approach to promote the ISC process involves augmenting the spin-orbit coupling (SOC) of the PS through the incorporation of heavy atoms or specific organic groups [24]. However, this approach still inevitably has some drawbacks and limitations, such as dark toxicity. Recently, self-assembly driven by aggregation-induced emission (AIE) has emerged as a promising technique for crafting functional materials at the molecular scale [25], offering several benefits in phototherapy: (1) This aggregation-induced self-assembly (AISA) shields internal monomer molecules from oxidation and degradation, thereby significantly enhancing the photostability of PSs [26]. (2) Leveraging the confinement mechanism of intramolecular motion (RIM), AISA can mitigate non-radiation relaxation, thereby facilitating the ISC process [27,28]. By harnessing the benefits of AIE and integrating them with Ir(III) complexes known for their high ISC efficiency, innovative PSs can be developed to optimize the generation of ROS and improve the therapeutic efficacy of PDT.

To maximize the efficiency of PDT, we proposed an organelle-targeted aggregation-induced enhanced photodynamic therapy (AIE-PDT) strategy. As a proof of concept, we synthesized a mitochondrial-targeting metal-based PS Ir-TPE (Scheme 1) with superior photodynamic properties by incorporating mitochondria-targeting AIEgens into an Ir(III) complex with high ROS production. AIE prevents PS aggregation-caused quenching and boosts ROS generation, while mitochondrial targeting enhances ROS production within mitochondria, leading to enhanced therapeutic effects. Compared to single-functional Ir-NH_2 and AIEgen (TPE-PPh_3), Ir-TPE displayed high ROS production and cancer cell selectivity in an aqueous solution. Cell imaging and ICP-MS experiments revealed that Ir-TPE localized in mitochondria exhibited significant phototoxicity to human breast cancer MCF-7 cells under visible light. Mechanistic studies explored ROS generation, mitochondrial damage, autophagy induction, and ferroptosis by Ir-TPE in PDT. Finally, efficacy was confirmed in a mouse tumor model, validating the reliability of the organelle-targeted AIE-PDT strategy.

Our previous investigation [29] revealed that the Ir(III) complex Ir-NH_2, a cyclometalated compound, possesses the remarkable capacity to inflict mitochondrial harm and trigger autophagy under dark conditions, effectively eliminating cancer cells. Nevertheless, this complex exhibits an identical lethality towards normal cells, and its light-induced ROS production is inadequate, rendering its phototoxicity unsatisfactory. Alternatively, the tetraphenyl ethylene (TPE) derivative modified with triphenylphosphine (TPE-PPh_3) boasts exceptional AIE performance and mitochondrial targeting proficiency [30,31]. However, it also exhibits notable dark toxicity and lacks selectivity in discriminating between normal and cancer cells. To address these challenges, we attempted to combine these two compounds and designed a photosensitizer with mitochondrial targeting ability, aiming to enhance the photodynamic efficiency of the cyclometalated Ir(III) complex through AIE-PDT strategy. By doing so, we hope to mitigate the dark toxicity towards cells by reducing the required drug dosage.

Ir-NH_2 and TPE-PPh_3 were prepared according to the reported procedures [29,30], Ir-TPE were synthesized as shown in Scheme S1 (Supporting information), and the structures were fully characterized using ^1H NMR, ^{13}C NMR, ESI-MS, and HR-MS, as shown in Figs. S1–S8 (Supporting information).

The photophysical properties of Ir-TPE, Ir-NH_2 and TPE-PPh_3 were studied. The UV–vis and photoluminescence (PL) spectra of Ir-TPE, Ir-NH_2 and TPE-PPh_3 in DMSO/PBS (v/v, 1/99) were shown in Fig. 1a and Fig. S9 (Supporting information). Ir-TPE exhibited main absorption peaks attributed to the metal–ligand charge transition (MLCT) at the range from 250 nm to 500 nm, while Ir-NH_2 at the range from 250 nm to 380 nm, which showed that Ir-TPE can be excited by visible light to generate ROS. The PL emission peaks of TPE-PPh_3, Ir-NH_2, and Ir-TPE are located around 475, 610, and 580 nm, respectively (Fig. S9 in Supporting information). These results indicated that the complex Ir-TPE has good photophysical properties and can be used for further biological applications.

The AIE properties of Ir-TPE were further examined. Ir-TPE showed weak fluorescence in DMSO, while the fluorescence intensity was significantly enhanced upon the addition of water, indicating that Ir-TPE owned obvious AIE properties (Fig. 1b). With the increase of the content of the bad solvent, *e.g.*, H_2O, the fluorescence intensity increased significantly, which was attributed to the restriction of RIM due to the aggregation. We also tested the AIE properties of two precursor compounds, Ir-NH_2 and TPE-PPh_3, and showed that TPE-PPh_3 has excellent AIE properties, while Ir-NH_2 exhibits aggregation-caused quenching (ACQ) (Fig. S10 in Supporting information). Due to the hydrophobicity of the Ir-NH_2 moiety and the hydrophilicity of the PPh_3 group, the resulting amphiphilic complex Ir-TPE can spontaneously form aggregates in aqueous solution by self-assembly [32,33]. As shown in Fig. 1c, transmission electron microscopy (TEM) and dynamic light scattering (DLS) were subsequently examined to investigate the aggregated Ir-TPE in aqueous solution. The Ir-TPE nanoaggregates were observed with the size range of 32.7–91.3 nm in agreement with the DLS observation with the solvent of DMSO/H_2O (v/v, 1/9). In addition, we used the fluorescence spectrometry to determine the critical micelle concentration (CMC) of the solution by measuring the fluo-

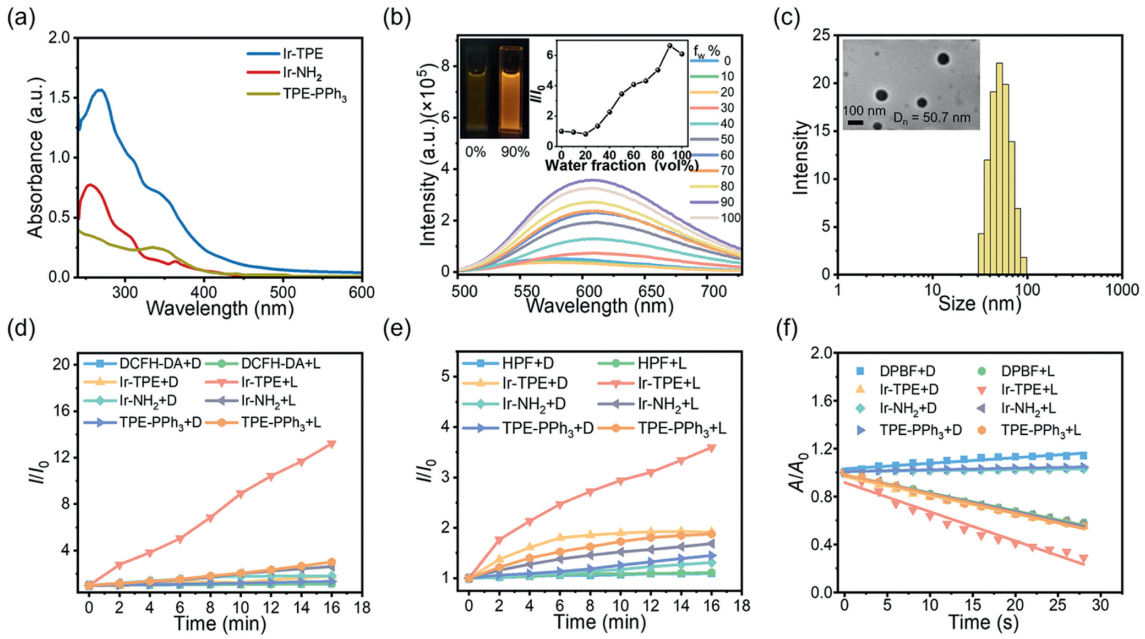

Fig. 1. (a) Absorption spectra of the compounds (20 μmol/L) in DMSO/PBS (v/v, 1/99). (b) Fluorescence spectra of Ir-TPE in DMSO/H_2O mixtures with various ratios (Left inset: the image of Ir-TPE in DMSO/H_2O mixtures upon 365 nm light irradiation. DMSO:H_2O = 100:0, 10:90 from left to right. Right inset: the intensity of Ir-TPE with the different water fraction). (c) DLS characterization of Ir-TPE (100 μmol/L) nanoparticles in DMSO/H_2O (v/v, 1/9) (Inset: TEM image of Ir-TPE). Time-course plots of DCFH (d), HPF (e) and DPBF (f) in the presence of different compounds under light irradiation (420 nm, 20 mW/cm^2).

rescence spectra of pyrene in Ir-TPE solution at different concentrations (Fig. S11 in Supporting information). This confirmed that Ir-TPE has excellent AIE properties and can form nanoaggregates in aqueous solution.

As shown in Fig. 1d and Fig. S12 (Supporting information), the ROS generation capacity of Ir-TPE, Ir-NH_2 and TPE-PPh_3 with or without light irradiation (420 nm, 20 mW/cm^2) in the DMSO/PBS (1/99, v/v) was subsequently evaluated using commercial 2′,7′-dichlorodihydrofluorescein diacetate (DCFH-DA) as a total ROS indicator. As the light exposure time increases, only the emission peak at 525 nm (attributed to the oxidation product DCF of DCFH-DA) was significantly enhanced in the solution containing Ir-TPE, which increased 13-fold after 16 min of irradiation. When Ir-NH_2 and TPE-PPh_3 were employed, however, the fluorescence of the DCFH-DA solution subtlety changed, suggesting the ROS generation efficacy of Ir-TPE aggregates is distinctly higher than Ir-NH_2 and TPE-PPh_3 in the aqueous solution. To clarify the specific type of ROS, various fluorescent probes including 2-hydroxyethidium (DHE, for $O_2^{\bullet-}$ detection), hydroxyphenyl fluorescein (HPF, for $^{\bullet}OH$ detection), and 3-Diphenylisobenzofuran (DPBF, for $^1O_2$ detection) were introduced. As shown in Fig. 1e and Fig. S13 (Supporting information), the fluorescence intensity of HPF at 515 nm sharply rose in the presence of Ir-TPE under light, which indicated that Ir-TPE possessed the type I ROS generation ability. Compared with Ir-NH_2 and TPE-PPh_3, in the presence of Ir-TPE, the absorbance of DPBF at 413 nm decreased most significantly when Ir-TPE is irradiated at 420 nm, indicating more $^1O_2$ is produced (Fig. 1f and Fig. S14 in Supporting information). We also calculated the $^1O_2$ quantum yield of Ir-TPE to be 0.83, which is higher than the standard material $\Phi_{Ru(bpy)3Cl2} = 0.74$. However, the fluorescence of DHE at 610 nm was almost constant in the presence of Ir-TPE, indicating that it does not produce $O_2^{\bullet-}$ (Figs. S15 and S16 in Supporting information). As shown in Figs. S17 and S18 (Supporting information), to demonstrates aggregation-enhanced ROS production, we further supplemented ROS testing in DMSO solvent. In the aggregated state, the emission peak increased by 13 times after 16 min of irradiation. However, in the pure DMSO, the increase was only about 2-fold. It demonstrated that aggregation could enhance the PDT efficacy of Ir-TPE by enhancing ROS production. Based on this, we further verified that the ROS type was measured using electron spin resonance (ESR), as shown in Fig. S19 (Supporting information). 2,2,6,6-Tetramethylpiperidine (TEMP) and 5,5-dimethyl-1-pyrroline-*N*-oxide (DMPO) were used as spin capture agents for $^1O_2$ and $^{\bullet}OH$, respectively. As mentioned previously, the characteristic ESR signals of $^1O_2$ and $^{\bullet}OH$ were observed for Ir-TPE upon illumination, which enhanced with longer exposure time. To analyze the stability of the formed nanoparticles, we tested the UV–vis absorption spectra of the complex in the DMSO/PBS (v/v, 1:99) (Fig. S20 in Supporting information). Even incubation for up to 72 h, there was no obvious change in absorption intensity and shift in absorption position, indicating that the Ir-TPE nano aggregates were relatively stable under certain conditions. These results above revealed that Ir-TPE nano aggregates can significantly elevate type I and type II ROS generation at the same time compared to Ir-NH_2, which preliminarily validated the potential of aggregation-enhanced ROS production for PDT. Moreover, the Ir-TPE nano aggregates will remain stable during long-term storage in PBS.

Next, we investigated the properties of Ir-TPE in cells. The entry of Ir-TPE into MCF-7 cells was studied by a confocal laser scanning microscope (CLSM). With the prolongation of time, the fluorescence intensity of Ir-TPE gradually increased, and it is clear in the cell after 4 h (Fig. 2a), the time-dependence imaging indicated the complex entered MCF-7 cells easily. As shown in Fig. S21 (Supporting information), the cellular uptake assay indicated that Ir-TPE entered MCF-7 cells through an energy-dependent endocytosis pathway. The intracellular distribution of complexes is of important guiding value for studying the mechanism of action. To study the intracellular distribution of Ir-TPE, the localization and content of complexes in each organelle were tested by inductively coupled plasma–mass spectrometry (ICP-MS) and CLSM. The ICP-MS results showed that both Ir-TPE with light irradiation mainly distribute in mitochondria (Fig. 2b and Fig. S22 in Supporting information), which was consistent with the localization imaging.

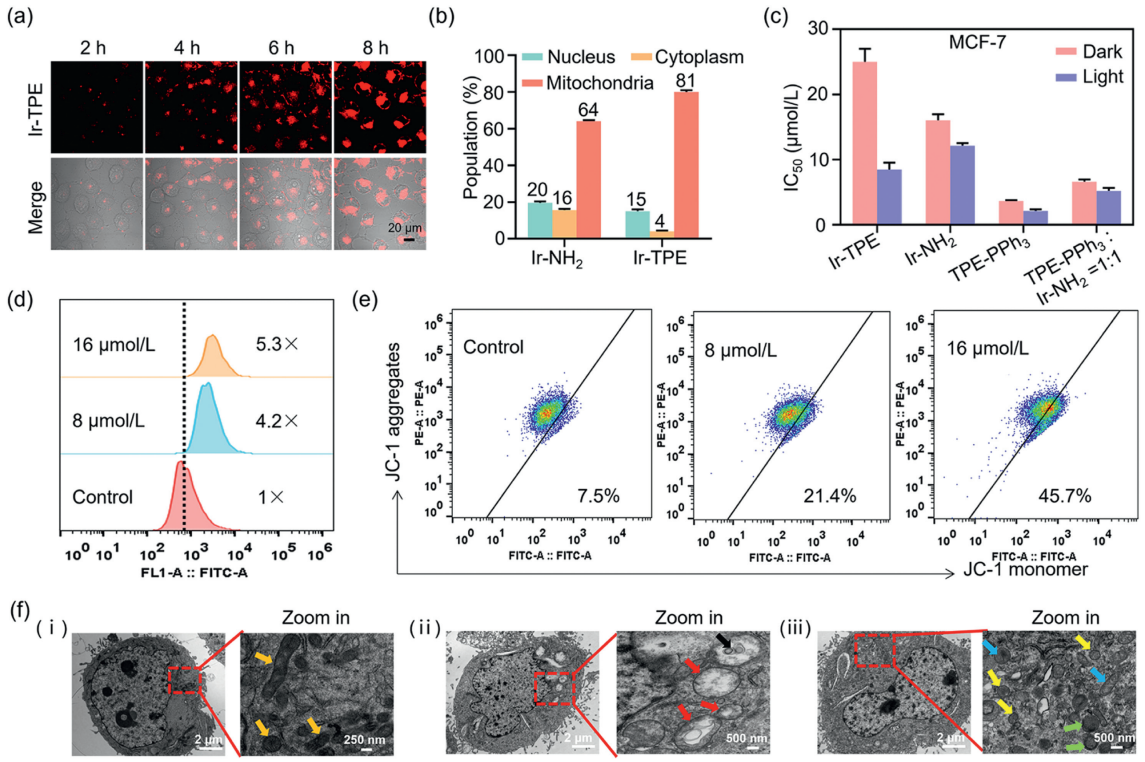

Fig. 2. (a) CLSM images of MCF-7 cells stained with 10 μmol/L Ir-TPE at different times. $\lambda_{ex} = 488$ nm. (b) Cellular uptake by different organelles of 10 μmol/L Ir-TPE and 10 μmol/L Ir-NH_2 under irradiation measured by ICP-MS. (c) The IC_{50} values of these compounds on MCF-7 cells under light and dark conditions. (d) ROS production determined by flow cytometry after treating MCF-7 cells with Ir-TPE under light. (e) Flow cytometry quantification of JC-1-labeled MCF-7 cells under light treated by Ir-TPE (8, 16 μmol/L) for 20 h. (f) TEM images of mitochondrial morphology under different conditions in MCF-7 cells. (i) DMSO + light (420 nm, 20 mW/cm^2) as control group, (ii) and (iii) Ir-TPE treatment with the light group. Data are shown as mean ± SD ($n = 3$).

Next, we studied the anti-proliferation activity of the complex. MTT assay was used to determine the cytotoxicity of Ir-NH_2 and Ir-TPE as well as cisplatin (CDDP) as the positive control against different cell lines, including cancer cells such as MCF-7 (human breast adenocarcinoma cell), MDA-MB-231 (triple negative breast cancer cell), A549 (human non-small cell lung cancer cell) and normal cells such as MCF-10A (human normal mammary epithelial cell), HLF (human lymphatic fibroblast).

The half-maximal inhibitory concentration (IC_{50}) values after 48 h of treatment are listed in Tables S1 and S2 (Supporting information). The comparison between the dark and light toxicity values, namely the photo-cytotoxicity index (PI), against different cell lines shows that Ir-TPE is highly toxic to MCF-7 cells. Among them, Ir-TPE exhibited the best inhibitory performance with an IC_{50} value of 8 μmol/L to MCF-7 cells under light (Table S1) with PI value as 3.1, suggesting Ir-TPE shows a better PDT effect than Ir-NH_2 and TPE-PPh_3 in MCF-7 cells. Therefore, we selected MCF-7 cells for subsequent experiments. Briefly, we found that Ir-TPE showed notably improved photodynamic performance after light exposure as shown in Fig. 2c and Table S2. At the same time, in normal cells, we were pleased to find that Ir-TPE was less toxic to MCF-10A cells compared to other control compounds (Table S2 and Fig. S23 in Supporting information), this is also the advantage of Ir-TPE.

To further explore the source of cellular phototoxicity, we tested ROS production using both fluorescence imaging and flow cytometry under light in cells, and the results showed that there was significant ROS production under light irradiation. Compared with the control group, the results of flow cytometry showed that indicated that Ir-TPE can produce 5-fold higher ROS in MCF-7 cells after light treatment (Fig. 2d). We also tested the ROS types in cells, which were consistent with those measured in solution, mainly $^1O_2$ and $^{\bullet}OH$ (Figs. S24 and S25 in Supporting information). As the dynamic center of cells, mitochondria play an important role in cell fate [34]. Due to the excellent mitochondrial targeting ability of the complex, we further tested the effects of the complex on mitochondrial function. Firstly, we investigated mitochondrial membrane potential (MMP), which is the basic characteristic that reflects mitochondrial integrity, with a mitochondrial membrane potential detection kit using CLSM and flow cytometry. As shown in Fig. S26 (Supporting information), the red fluorescence in the light group was decreased, and the green fluorescence enhancement indicated the depolarization of mitochondria. We further analyzed the changes in MMP using flow cytometry as depicted in Fig. 2e, the monomer fraction in the light-treated group increased significantly with concentration dependence from 7.5% to 45.7%. The large production of ROS and the significant decrease of MMP indicate that the function of mitochondria is significantly destroyed, so the morphology of mitochondria is bound to be severely affected.

High ROS levels led to oxidative damage to DNA [35,36]. The effect of Ir-TPE on the expression of γ-H2AX in MCF-7 cells was examined, Ir-TPE could significantly increase the expression of γ-H2AX in MCF-7 cells, and it was also found that when ROS inhibitor *n*-acetyl-cysteine NAC was added, γ-H2AX expression levels in MCF-7 cells were suppressed after Ir-TPE treatment (Fig. S27 in Supporting information), suggesting that Ir-TPE induced DNA damage was caused by excessive oxidative stress. Cell cycle arrest was also induced by DNA damage. The results showed that Ir-TPE inhibited MCF-7 cells proliferation mainly by blocking the cell cycle in the G2/M phase (Figs. S28 and S29 in Supporting information).

We further used TEM to observe whether the mitochondrial morphology changed in MCF-7 cells. As shown in Fig. 2f, mitochondria from MCF-7 cells showed clear mitochondrial bilayers and crista structures in the control group (orange arrow) groups. As we expected, in the Ir-TPE treatment with the light group, the mito-

chondria swelled (red arrow) companying with the disappeared internal crista, at the meantime, autolysosome (black arrow), which is the characteristic of mitophagy. In addition to this, we also found that some mitochondria wrinkled (yellow arrow), bilayer membrane density increased (green arrow), and broken mitochondria (blue arrow), indicating ferroptosis. These results all indicated that under light, Ir-TPE produced sufficient ROS by AIE-PDT effect, thus destroying mitochondrial integrity and resulting in mitochondrial damage.

The above studies suggest that Ir-TPE can be used as an effective PDT drug. To clarify the cell death pathways involved in this PDT process, we then determined the cell viability of MCF-7 cells co-incubated with different cell death inhibitors and Ir-TPE under short periods of light exposure (Fig. 3a). MTT assay revealed that only the ferroptosis inhibitor (ferrostatin-1, Fer-1) and autophagy inhibitor (chloroquine, CQ) rather than the inhibitors of apoptosis (z-VAD-fmk) and necrosis (necrostatin-1, Nec-1) resulted in a notable viability enhancement, suggesting ferroptosis and autophagy might be the main cell death pathway induced by Ir-TPE *via* light irradiation, which consistent with the mitochondrial behavior shown by TEM (Fig. 2f). Above all, photoirradiated Ir-TPE can trigger multiple cell death modes by inducing mitophagy and ferroptosis.

Previous results indicated that Ir-TPE can induce mitophagy. Therefore, we further confirmed the phenomenon of autophagy in cells. Initially, the results of protein immunoblotting experiments showed an increase in LC3-II levels and LC3-II/LC3-I ratio in the control group. The upregulation of PINK1 and Parkin protein expression also indicated mitochondrial damage-induced mitophagy as depicted in Figs. 3b and c. To visually validate this result, autophagy was observed in cells treated with Ir-TPE by confocal microscopy [37]. As shown in the confocal images of Fig. S30 (Supporting information), the green fluorescence of LC3B was observed under the irradiation conditions of the Ir-TPE group, implying the occurrence of autophagy in the cells. All these results illustrated that Ir-TPE leads to mitophagy in cancer cells *via* autophagosomes and lysosome fusion, as shown in Fig. 3d.

Ferroptosis is the other major mode of cell death accompanied by the accumulation of lipid peroxidation, which was then monitored using C11-BODIPY as a lipid peroxidation probe [38,39]. Confocal imaging showed that Ir-TPE significantly enhanced the probe's fluorescence under light irradiation conditions (Fig. 3e), indicating a marked accumulation of lipid peroxidation. Meanwhile, ferroptosis inhibits cystine/glutamate antiporter (system Xc^-) activity [40,41], depletes GSH and ultimately inhibits glutathione peroxidase 4 (GPX4) [42], as shown in Fig. 3f, the GSH content after light exposure was lower than that control group, in verse, the GSSG (oxidized GSH) content was increased, resulting in the elevated GSSH/GSH (Fig. S31 in Supporting information) [43]. Subsequently, Western blot analysis showed that Ir-TPE inhibited the expression of the lipid peroxidase scavenger GPX4, which may also lead to lipid ROS accumulation and ultimately ferroptosis (Figs. 3g and h). Furthermore, photo-irradiating Ir-TPE downregulated the expression of SLC7A11 protein (part of the system Xc^- transporter) [44]. According to literature reports [45,46], the ROS level is closely related to the expression of SLC7A11 protein, and it was also found that the expression level of SLC7A11 protein was significantly upregulated after the addition of ROS scavenger NAC, indicating that the inhibition of SLC7A11 protein was caused by oxidative stress (Fig. S32 in Supporting information). And, we confirmed that Ir-TPE induced the ferroptosis involving the system Xc^--GSH-GPX4 pathway (Fig. 3i).

Since Ir-TPE showed excellent anti-proliferative properties of 2D monolayer MCF-7 cells, 3D multicellular tumor spheroids (3D MCTSs) were used to simulate solid tumors, and then the performance of Ir-TPE treatment was evaluated, As shown in Fig. S33a

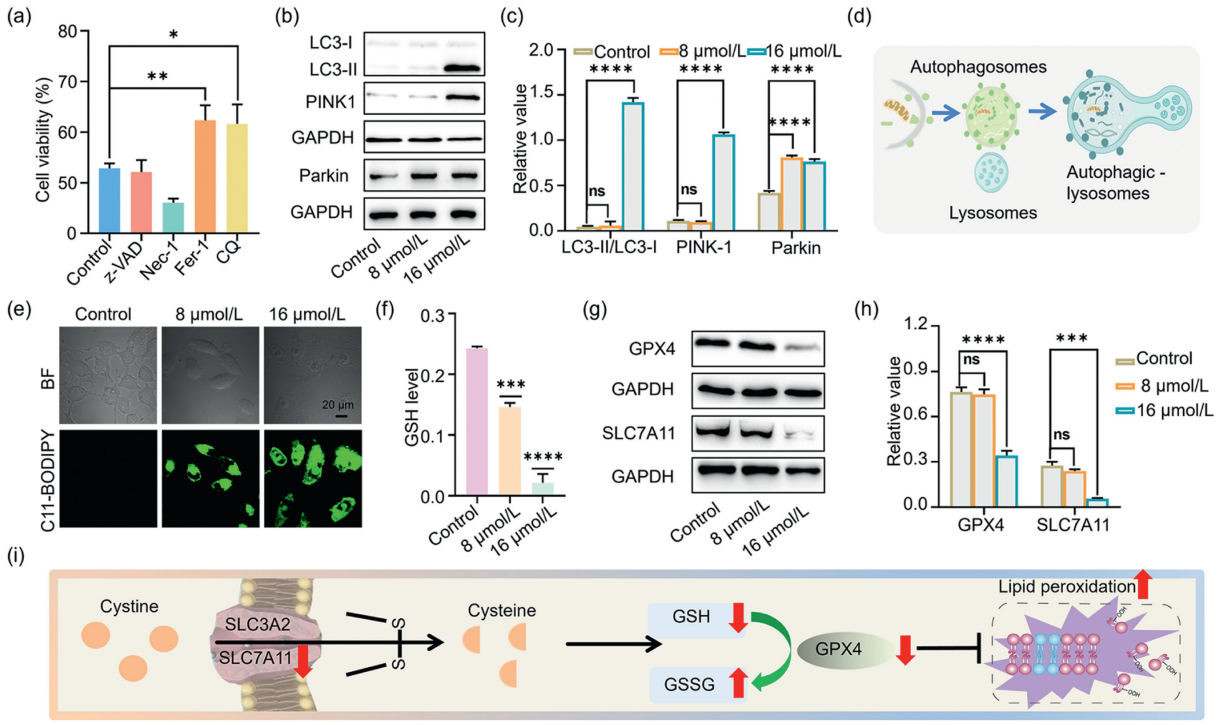

Fig. 3. (a) The cell viability with different death inhibitor treatments under light exposure. (b) The immunoblotting of autophagy associated proteins in MCF-7 cells treated with Ir-TPE (8, 16 μmol/L) under light. (c) Quantitative analysis of autophagy-related proteins from (b). (d) The mechanism illustration of autophagy induction by autophagosome and lysosome fusion. (e) Confocal imaging of MCF-7 cells stained with C11-BODIPY after Ir-TPE treatment under light. (f) The GSH levels in MCF-7 cells after different treatments. (g) The immunoblotting of ferroptosis related proteins in MCF-7 cells treated with Ir-TPE (8, 16 μmol/L) for 44 h under light. (h) Quantitative analysis of ferroptosis-related proteins from (g). (i) The ferroptosis pathway induced by photo-irradiated Ir-TPE. Data are shown as mean ± SD ($n = 3$).

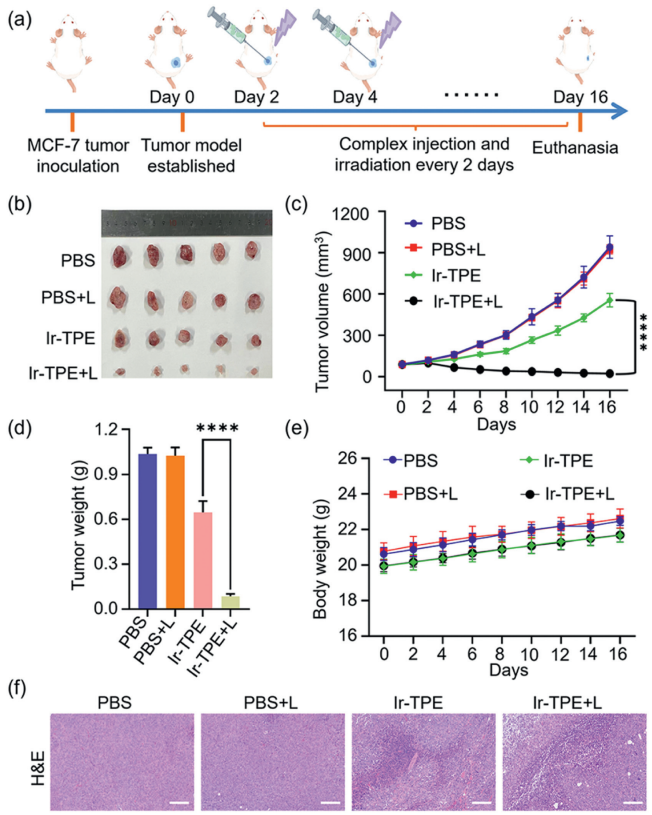

Fig. 4. (a) Schematic illustration of *in vivo* phototherapeutic protocol mediated by Ir-TPE. (b) Tumor photos at the end of the treatment period in different groups. (c) Time-dependent tumor growth curves after treatment. (d) Tumor weight of mice after the last determination, $^{****}P < 0.0001$. (e) Body weight variations during the treatment. (f) The H&E analysis of tumor tissues after treatment with different drugs. Scale bar = 100 μm. Data are shown as mean ± SD ($n = 5$).

(Supporting information). After MCF-7 cells were cultured for 6 days, the diameter of spheroids in the Ir-TPE-treated light-treated group was significantly reduced, while the spheroid growth in the control group showed no significant inhibitory effect, indicating that light-treated Ir-TPE has potent anti-proliferative activity against 3D MCF-7 MCTSs. In addition, we also use calcein AM (green fluorescence for living cells detection) and PI (propidium iodide) (red fluorescence for dead cell detection) double staining methods to assess the cell of MCTs survival after Ir-TPE treatment. As shown in Fig. S33b (Supporting information), compared with the strong green fluorescence of MCTSs in the control group, the green fluorescence in Ir-TPE-treated MCTSs after light exposure was significantly reduced and the red fluorescence was significantly enhanced, indicating that the viability of MCF-7 cells was significantly reduced. These results indicated that photoactivated Ir-TPE can effectively inhibit the proliferation of 3D MCTSs and is a promising PS for PDT.

Encouraged by the promising outcomes of the *in vitro* studies, we proceeded to assess the *in vivo* anti-tumor effects of Ir-TPE on MCF-7 tumor-bearing mouse models. All of the animal experiments were approved by the University Animal Care and Use Committee of Nanjing Normal University (the accreditation number, SYXK-(Su) 2020-0047). As shown in Fig. 4a, the tumor-bearing BALB/c mouse model was established by subcutaneously inoculating MCF-7 cells. The tumor-bearing mice were randomly divided into four groups and orthotopic injection with Ir-TPE (5 mg/kg mice weight) and PBS buffer solution once every two days. After 16 days' treatment, as shown in Figs. 4b-d the growth of the tumors was significantly inhibited after the mice were treated with Ir-TPE under light exposure. Additionally, like the PBS buffer solution groups, the mice treated with Ir-TPE did not show significant changes in body weight during cancer treatment (Fig. 4e).

Previous studies have validated the effectiveness of Ir-TPE combined with light irradiation in suppressing tumor growth. To elucidate the mechanism *in vivo*, we employed Hematoxylin and Eosin (H&E) staining, terminal deoxynucleotidyl transferase dUTP nick-end labeling (TUNEL) staining, and Ki67 (a nuclear protein related to cell proliferation) immunohistochemical staining to analyze the histological alterations. As evident in Fig. 4f, H&E staining revealed marked nuclear shrinkage and a considerable reduction in area in tumor tissue of mice treated with Ir-TPE under light exposure, indicating a high degree of cell death induced by Ir-TPE. Conversely, the control group displayed no notable tumor necrosis. Subsequently, TUNEL staining assays demonstrated a substantial level of cell death in the tumor tissue of mice treated with Ir-TPE + light, indicating damage to a majority of tumor cells (Fig. S34a in Supporting information). In contrast, the control group showed no significant tumor necrosis. To assess cell proliferation, Ki67 immunohistochemical staining was performed, revealing a significant inhibition of cell proliferation, thus slowing down tumor growth. Additionally, we conducted *in vivo* immunofluorescence experiments to investigate the expression of specific pathway proteins. As illustrated in Fig. S34b (Supporting information), an enhanced purple fluorescence of LC3 protein and a diminished red fluorescence of GPX4 and green fluorescence of SLC7A11 protein were observed in the Ir-TPE + light group, indicating that Ir-TPE exhibits anti-tumor properties *in vivo* by inducing ferroptosis and autophagy. Finally, the safety of different organs and using the therapeutic method was evaluated by H&E staining. It is worth noting that in mice treated with Ir-TPE, there were no obvious organ injuries or pathological changes in the five major organs, which was consistent with the control group (Fig. S35 in Supporting information). Ir-TPE has minimal systematic toxicity small side effects and good biocompatibility. These findings suggested the success of the Ir(III)-based PDT for *in vivo* treatment.

In summary, we present a strategy for organelle-targeted and AIE-PDT. To demonstrate its feasibility, we have designed and synthesized a mitochondria-targeting cyclometalated Ir(III) complex, Ir-TPE, which exhibits an aggregation-enhanced photodynamic effect, triggers ferroptosis and autophagy for cancer therapy. This complex self-assembles into nanoaggregates in aqueous solution, generating a significant amount of ROS upon light irradiation. Cytotoxicity experiments demonstrate the high photo-cytotoxicity of Ir-TPE towards irradiated cells. Confocal imaging and ICP-MS analysis reveal that the complex preferentially accumulates in mitochondria. *In vitro* studies demonstrate that light-irradiated Ir-TPE triggers mitophagy by generating ROS to damage mitochondria. Additionally, Ir-TPE inhibits GSH production and promotes ferroptosis upon light exposure, ultimately engaging multiple cell death mechanisms. Furthermore, we demonstrate the effective inhibition of 3D MCTS proliferation and *in situ* tumor ablation *in vivo* using this complex. This study validates our proposed strategy and highlights the potential of AIE-based complexes in expanding their applications in diagnosis and treatment.

Declaration of competing interest

The authors declare that they have no known competing financial interests or personal relationships that could have appeared to influence the work reported in this paper.

CRediT authorship contribution statement

Panpan Wang: Writing – original draft, Formal analysis, Data curation. **Hongbao Fang:** Writing – review & editing, Writing –

original draft, Supervision, Project administration, Conceptualization. **Mengmeng Wang:** Formal analysis, Data curation. **Guandong Zhang:** Visualization, Data curation. **Na Xu:** Visualization, Data curation. **Yan Su:** Visualization, Validation, Formal analysis. **Hongke Liu:** Project administration, Conceptualization. **Zhi Su:** Writing – review & editing, Supervision, Project administration, Funding acquisition.

Acknowledgments

We appreciate the financial support from the National Natural Science Foundation of China (Nos. 22277056, 21977052), the Distinguished Young Scholars of Jiangsu Province (No. BK20230006), the Natural Science Foundation of Jiangsu Province (Nos. BK20230977, BK20231090), the Natural Science Foundation of the Higher Education Institutions of Jiangsu Province (No. 23KJB150020), and the Jiangsu Excellent Postdoctoral Program (No. 2022ZB758).

Supplementary materials

Supplementary material associated with this article can be found, in the online version, at doi:10.1016/j.cclet.2024.110099.

References

[1] D.W. Felsher, Nat. Rev. Cancer 3 (2003) 380–387.
[2] M.P. Murphy, R.C. Hartley, Nat. Rev. Drug Discov. 17 (2018) 865–886.
[3] Z. Zhou, J. Song, L. Nie, et al., Chem. Soc. Rev. 45 (2016) 6597–6626.
[4] M. Lan, S. Zhao, W. Liu, et al., Adv. Healthc. Mater. 8 (2019) 1900132.
[5] X. Wang, J. Qian, Z. Yang, et al., Adv. Mater. 36 (2024) 2310964.
[6] H. Yuan, Z. Han, Y. Chen, et al., Angew. Chem. Int. Ed. 60 (2021) 8174–8181.
[7] T.C. Pham, V.N. Nguyen, Y. Choi, et al., Chem. Rev. 121 (2021) 13454–13619.
[8] C. Bloyet, F. Sciortino, Y. Matsushita, et al., J. Am. Chem. Soc. 144 (2022) 10830–10843.
[9] H. Wang, Q. Li, P. Alam, et al., ACS Nano 17 (2023) 14347–14405.
[10] S. Monro, K.L. Colón, H. Yin, et al., Chem. Rev. 119 (2018) 797–828.
[11] S. Abdolmaleki, A. Aliabadi, S. Khaksar, Coord. Chem. Rev. 501 (2024) 215579.
[12] S. Gan, W. Wu, G. Feng, et al., Small 18 (2022) 2202242.
[13] Y. Wu, S. Li, Y. Chen, et al., Chem. Sci. 13 (2022) 5085–5106.
[14] F.E. Poynton, S.A. Bright, S. Blasco, et al., Chem. Soc. Rev. 46 (2017) 7706–7756.
[15] L. Zhang, Y. Li, W. Che, et al., Adv. Sci. 6 (2019) 1802050.
[16] A. Zamora, G. Vigueras, V. Rodríguez, et al., Coord. Chem. Rev. 360 (2018) 34–76.
[17] W. Lv, Z. Zhang, K.Y. Zhang, et al., Angew. Chem. Int. Ed. 55 (2016) 9947–9951.
[18] J.Y. Zhua, A. Ouyang, Z.L. Shen, et al., Chin. Chem. Lett. 33 (2022) 1907–1912.
[19] J.L. Tong, X.Y. Yang, X.X. Song, et al., Dalton Trans. 52 (2023) 1105–1112.
[20] X.Z. Cai, K.N. Wang, W. Ma, et al., J. Nanobiotechnol. 19 (2021) 254.
[21] Q. Yang, H.Y. Jin, Y.C. Gao, et al., ACS Appl. Mater. Inter. 11 (2019) 15417–15425.
[22] W. Wu, X. Shao, J. Zhao, et al., Chem. Rev. 4 (2017) 1700113.
[23] X. Xing, P. Zhu, E. Pang, et al., Chin. Chem. Lett. 35 (2024) 109452.
[24] Y.F. Kang, W.K. Chen, K.X. Teng, et al., CCS Chem. 4 (2022) 3516–3528.
[25] J. Wang, Y. Wang, Z. Li, et al., Chin. Chem. Lett. 35 (2024) 108934.
[26] P. Cen, J. Huang, C. Jin, et al., Aggregate 4 (2023) e352.
[27] C. Li, Y. Gao, R. Huang, et al., ACS Mater. Lett. 4 (2022) 657–664.
[28] H. Ma, S. Long, J. Cao, et al., Chem. Sci. 12 (2021) 13809–13816.
[29] M.M. Wang, F.J. Xu, Y. Su, et al., Angew. Chem. Int. Ed. 61 (2022) e202203843.
[30] Y. Su, H. Lin, Y. Tu, et al., Chem. Sci. 13 (2022) 1428–1439.
[31] J. Zielonka, J. Joseph, A. Sikora, et al., Chem. Rev. 117 (2017) 10043–10120.
[32] S.W. Wang, K.Z. Gu, Z.Q. Guo, et al., Adv. Mater. 18 (2018) 1805735.
[33] H.B. Cheng, Y.Y. Li, B.Z. Tang, et al., Chem. Soc. Rev. 49 (2020) 21–31.
[34] Z. Yu, X. Luo, C. Zhang, et al., Chin. Chem. Lett. 35 (2024) 109519.
[35] M. Schieber, N.S. Chandel, Curr. Biol. 24 (2014) R453–R462.
[36] U.S. Srinivas, B.W.Q. Tan, B.A. Vellayappan, et al., Redox Biol. 25 (2019) 101084.
[37] M. Lazarou, D.A. Sliter, L.A. Kane, et al., Nature 524 (2015) 309–314.
[38] H. Feng, B.R. Stockwell, PLoS Biol. 16 (2018) e2006203.
[39] J. Zhuang, B. Wang, H. Chen, et al., ACS Nano 17 (2023) 9110–9125.
[40] X.X. Peng, H. Zhang, R. Zhang, et al., Angew. Chem. Int. Ed. 62 (2023) e202307838.
[41] S. Li, H. Yuan, Y. Chen, et al., Fundam. Res. 3 (2023) 525–528.
[42] L. Li, B. Sun, J. Sun, et al., Chin. Chem. Lett. 35 (2024) 109538.
[43] X. Zhao, J. Zhang, W. Zhang, et al., Chem. Sci. 14 (2023) 1114–1122.
[44] P. Koppula, L. Zhuang, B. Gan, Protein Cell 12 (2021) 599–620.
[45] P. Koppula, Y.L. Zhang, L. Zhuang, B. Gan, Cancer Commun. 38 (2018) 1–13.
[46] S.Y. Ding, X.Y. Duanmu, L.S. Xu, L. Zhu, Z.Q. Wu, Biomed. Pharmacother. 165 (2023) 115185.